EEET ECOLOGICAL ENGINEERING & ENVIRONMENTAL TECHNOLOGY

Ecological Engineering & Environmental Technology 2024, 25(9), 26–36
https://doi.org/10.12912/27197050/189889
ISSN 2299–8993, License CC-BY 4.0

Received: 2024.05.25
Accepted: 2024.07.10
Published: 2024.08.01

Estimating Soil Parameters Using C Band Synthetic Aperture Radar in Laylan, Iraq

Chelar Awny Ali[1*], Muntadher Aidi Shareef[1], Qahtan A.M. Al Nuaimy[1]

[1] Technical Engineering College, Northern Technical University, Kirkuk, Iraq
* Corresponding author's e-mail: chelar.awnygs@ntu.edu.iq

ABSTRACT

This study aims to develop models for estimating topsoil properties by analyzing both the parametric and textural features extracted from Sentinel-1 C-SAR (VV, VH) images. Field measurements were collected from 13 soil samples in the Laylan region of Kirkuk City, Iraq, and utilized to develop and validate the models. The study employed classification algorithms, including the random forest (RF) and maximum likelihood (ML) classifiers, using specific indicators derived from Sentinel-1 data. Additionally, a soil triangle was constructed using three axes to represent the predicted target parameters, facilitating the identification of five distinct soil groups in the study area. The findings reveal that the soil triangle enables the delineation of five subcategories of soil characterized by varying proportions of sand and silt. Each soil sample was categorized into one of five predefined classes based on its clay content, ranging from 0% to 14.48%. The performances of the ML and RF algorithms were assessed, demonstrating their effectiveness in estimating percentage labels despite limited training data, with ML exhibiting higher accuracy than RF. The developed models showed promising potential; however, their applicability should be tested across diverse geographic regions with varying climatic conditions. Future research could focus on utilizing these models to generate soil texture maps, potentially enhancing soil parameter estimation in different environments.

Keywords: SAR images, Sentinel-1, random forest, soil texture, linear regression model.

INTRODUCTION

Accurate soil parameter estimation is essential for land management, agriculture, and environmental monitoring. Traditional soil analysis methods are labor-intensive, time-consuming, and have limited spatial coverage. The Laylan area in Kirkuk City, Iraq, poses challenges due to diverse soil types and varying climatic conditions. Advanced remote sensing techniques, specifically C Band Synthetic Aperture Radar (SAR) images, can provide a more efficient and comprehensive solution.

Estimating and retrieving soil parameters from C-band synthetic aperture radar (SAR) images using parametric and textural analysis is challenging in remote sensing, as highlighted by (Liao et al., 2013). The majority of current approaches rely on costly, time-consuming ground-based measurements that are geographically constrained. These limitations, coupled with time constraints and depositional variability, make precise data collection and analysis of soil texture parameters difficult. Fields such as agricultural and environmental management heavily depend on fine-scale investigations of soil texture diversity (Liao et al., 2013). Ground measurements have traditionally been used to assess soil texture and water status. Still, they are deemed insufficient due to their cost, time consumption, and inability to monitor changes in soil moisture across space and time accurately. To increase the precision and breadth of soil observations for hydrological applications and water resource management, the scientific community has invested significantly in developing remote sensing products (Korres et al., 2015, Alexandridis et al., 2016). Over the past 30 years, remote sensing techniques, as noted by

(Ge et al.,2011, Yu et al., 2018), have emerged as valuable tools for studying soil characteristics and other earth resources. With its superior measurement capabilities, all-weather capability, penetrating capability, dielectric constant sensitivity, roughness, wavelength, and polarization, microwave remote sensing has advantages over optical and hyperspectral sensors. Previous studies, such as those by (Chang et al., 2003), have shown that soil textural and hydraulic qualities can be efficiently studied using soil moisture content, temperature, and brightness. SAR has demonstrated promise in measuring and tracking surface soil properties, particularly in examining soil moisture and roughness (Srivastava et al., 2009, Holah et al., 2005). (RS) imaging has successfully estimated soil properties with high accuracy and speed (Salahalden et al., 2024). The versatility and ability of SAR to penetrate all weather conditions make it useful for surface soil moisture monitoring (Kornelsen and Coulibaly, 2013). Moreover, the study aimed to utilize radar data from the Sentinel-1 satellite to evaluate the effectiveness of radar indicators in classifying soil texture. This research integrates field measurements and satellite observations in the Laylan region of Kirkuk City, Iraq, utilizing SAR images, specifically Sentinel-1 C-SAR (VV, VH). The images are analyzed through parametric and texture analysis to classify soil content. Sensitivity analysis of several soil texture indicators is conducted, followed by classification using RF and ML algorithms. The primary aim is to develop and validate models that combine parametric and texture analysis of Sentinel-1 C-SAR images, thereby enhancing soil assessment accuracy in the Laylan region.

MATERIAL AND METHODS

Study area

The study area is located in the city of Laylan, which is located inside the Kirkuk Governorate in north-central Iraq (Figure 1). The Laylan coordinates extend from longitude 44° 20’ to 44° 45’ and from latitude 35° 09’ to 35° 25’. The entire area of Laylan is approximately 691 km^2. It is of great economic importance because it is renowned for oil production. It is located approximately 255 kilometers from the capital, Baghdad, and approximately 19 kilometers from Kirkuk. Within its boundaries lies the Kirkuk Cement factory. The Jambur anticline serves as the region’s southwestern boundary, while the Kirkuk structure defines the northeastern boundary. The southern and southwestern boundaries are delineated by a transient watercourse named the Mamsha Stream, while the northwestern and western boundaries are demarcated by another temporary watercourse referred to as the Shireen Ephemeral Stream (Amin Beiranvand Pour, 2022). The elevation ranges from 243 meters to 402 meters in relation to sea level. (Amin Beiranvand Pour, 2022). The study area consists of two parts: the first is near residential areas, and the second is near the bor structure.

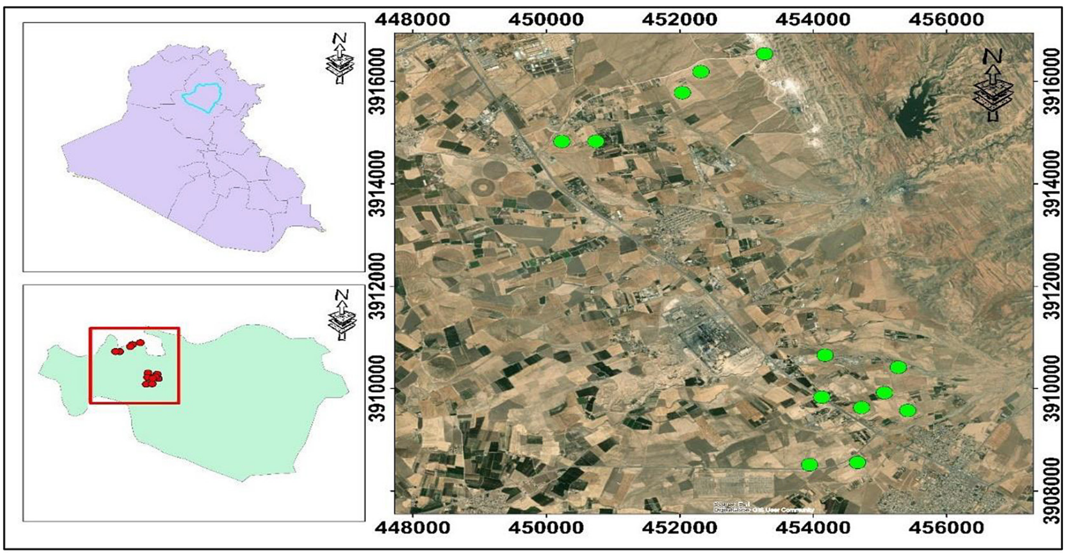

Figure 1. Location map of the studied area

Data used

Ground texture measurements

In this study, 13 soil samples at a depth of 30 cm are extracted from the research location and its surrounding areas to observe the soil moisture and texture (Figure 2). The samples were collected on exposed surfaces to showcase the ability of the SAR data to achieve satisfactory outcomes. The handheld GPS gadget accurately determined the coordinates with a margin of error of ± 3.6. An HS-5001EZ instrument is used to measure the moisture density meter to determine the dry density and water content in the study area. On the other hand, the physical characteristics of the soil are extracted after drying the samples in a laboratory oven at 100 degrees Celsius for 24 hours prior to laboratory analysis.

To assess the soil's texture, the soil samples with a diameter larger than 2 mm are removed, which represent the gravel fraction. We measured the sand, silt, and clay proportions of the soil samples using the hydrometer method, which relies on the rate of sediment settlement in a solution (Periasamy et al., 2021).

Satellite data (sentinel 1 SAR data)

The "Copernicus" program encompassed the launches of Sentinel-1A (S-1A) in April 2014 and Sentinel-1B in April 2016, with the primary objective of observing and monitoring the Earth's surface for environmental monitoring applications (Bousbih et al., 2019). These satellites operate at the C band (5.26 GHz) frequency and utilize four distinct modes, including the interferometric wide swath (IW) mode, which is specifically designed for land observations (Periasamy, 2018). The synthetic aperture radars (SARs) on these satellites enable data collection regardless of weather conditions, capturing images with polarizations such as VV, VH, HH, and HV (Bousbih et al., 2019). This investigation utilized data from the Sentinel-1 constellation acquired in early November 2023 in VV and VH polarizations. The data consisted of interferometric wide (IW) swath images with a wavelength of approximately 6 cm. To process the data, we performed a series of steps, including thermal noise removal, geometric correction, speckle filtering, and radiometric calibration, ultimately calculating the backscattering coefficient (Bousbih et al., 2019). The Characterization of Sentinel-1A image is detailed below, as illustrated in Figure 3.

Pre-processing for SAR imagery

Preprocessing methods have been employed to correct atmospheric and radiometric distortions in the images(Mahmoud et al., 2022).The

Figure 2. Different sampling sites in studied area

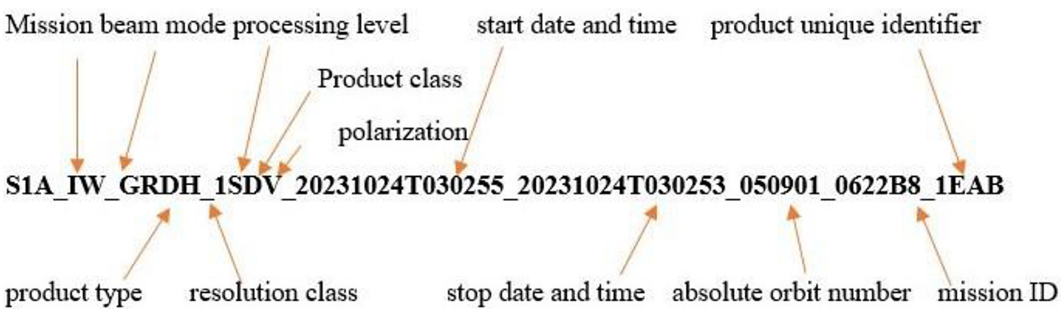

Figure 3. Characterization of Sentinel-1A

SAR imaging pre-processing methods underwent a comprehensive evaluation, as detailed in Dingle Robertson (Davidson, et al., 2020). The following steps were conducted in pre-processing order:

1. The orbit file (Sentinel-1 data) was utilized.
2. The radioactive strength was determined to convert radar backscattering into a radar cross-section (σ^0) (Equation 1), where the amplitude images of VV and VH underwent radiometric calibration using the calibration parameter A^2 σ.

$$\sigma^0 = \frac{DN\ 2}{A^2\ \sigma} \tag{1}$$

DN represents the digital number present in the SAR images. To obtain the backscattering coefficient (σ^0dB) in decibels (dB) (Equation 2), the logarithm is applied to σ^0.

$$\sigma^0 dB = 10.\, log_{10}\sigma^0 \tag{2}$$

3. Radiometric terrain flattening – surface topography has a considerable impact on the radiometric characteristics of SARs, as highlighted by (Loew and Mauser, 2007). Variations in topography can complicate the retrieval of geophysical characteristics from SAR data, as noted by (Souissi and Ouarzeddine, 2016). The proposed technique successfully reduced the influence of topographical variation in SAR imaging for both VV and VH polarizations, as demonstrated by (van Zyl et al., 1993).

The resulting backscattering values in the image represent solely soil and land cover properties, independent of surface geometry.

$$\sigma^0 corr = \sigma^0 \times \frac{sin\,\eta * cos\theta\alpha}{sin\,\eta^{\circ}} \tag{3}$$

The variable σ^0 corr signifies the backscattering coefficient adjusted for terrain effects. The variable η represents the local incidence angle from SAR imagery, while η°denotes the incidence angle of SAR imagery. The variable θα indicates the azimuth slope derived from the DEM data. To reduce uncertainty arising from substantial elevation variations during topographical adjustment to the reference surface, we implemented masking for shadow and layover areas. Terrain correction, also known as ortho-rectification, is the process of adjusting an image to a predetermined coordinate system and eliminating the distortions caused by the angle and terrain. Sigma naught (σ0) is a measurement that represents the average amount of backscatter from a target, which has been adjusted to account for the size of the illuminated region in a horizontal plane (Robertson et al., 2020). The initial processing phase for Sentinel-1 data involved utilizing orbit state vectors. Precise information on the sensor's position and the velocity of the platform it was mounted on was essential for accurately aligning image pixels with specific locations on the Earth's surface, as highlighted by (Loew and Mauser, 2007). The orbit state vectors, which describe the satellite's position and velocity, were obtained from the metadata. These vectors were then utilized to accurately determine the location of each image, as documented by (Robertson, 2020). Each image underwent several processing steps before obtaining the backscattering coefficient. This process included speckle filtering, geometric correction, radiometric calibration, and thermal noise removal, as outlined by (Bousbih et al., 2019).

Models used

Linear regression model

The fundamental objective of basic regression analysis is to assess the impact of a predictor variable on a specific outcome, as noted by (Zou et al., 2003). Conversely, correlation analysis aims to examine the strength and direction of the relationship between two independent variables, as also discussed by (Zou et al., 2003). In a simple regression model, the focus is on the dependent variable and the regression parameters, which exhibit a linear relationship. This model involves a single independent variable, denoted as Xi for subjects i = 1 through n. The outcome variable corresponding to the dependent variable is labelled accordingly. The model can be expressed as:

$$\sigma^0 corr = \sigma^0 \times \frac{sin\,\eta * cos\theta\alpha}{sin\,\eta^{\circ}} \tag{4}$$

$$Yi = a + bXi + ei \tag{5}$$

In this case, an is the intercept (y-axis), and b is the slope of the regression line; both are considered regression parameters. The null hypothesis states that the random error term e_i is uncorrelated, has a mean of 0, and has a constant variance.

The fundamental equation used for regression analysis is as follows:

$$Y = a + b \times XY \text{ (Shareef et al., 2014)} \tag{6}$$

Nonlinear regression model

Nonlinear regression shares the fundamental concept of regression analysis with linear regression. The nonlinear regression depends on the nonlinear dependence of the prediction equation on one or more unknown parameters, as highlighted by (Huang and He, 2022). Linear regression is often used to construct purely empirical models, whereas nonlinear regression comes into play when there are physical reasons to believe that the relationship between the response variable and the predictors follows a specific functional form. A nonlinear regression model has the form such as:

$$Yi = f(xi, \vartheta) + \epsilon i \; I = 1,..., n \tag{7}$$

where: Yi – the replies, f – a known function of the covariate vector $xi = (x_i1..., x_ik)T$, and $\theta = (\theta 1..., \theta P)$, T is the parameter vector, εi – a random error. Typically, we assume that i is uncorrelated, with a mean of zero and a constant variance.

Classification algorithm

Different categorization techniques have been applied to texture mapping in agricultural fields (Bousbih et al., 2019). These techniques connect a set of data samples to multiple class labels using the selected feature vector. The parameters for each classifier are calculated based on the training dataset. The classification of satellite images and other images is divided into two techniques: supervised and unsupervised (Mezaal et al., 2022).

Random forest classifier. Breiman (2001) introduced an ensemble system based on trees for classification and regression. The objective of ensemble learning is to enhance prediction accuracy by combining the outcomes of multiple learning algorithms, surpassing that of any individual model. Unlike pruning techniques, this approach generates numerous decision trees (Grimm et al., 2008). During the training phase, each distinct bootstrap sample generates a new tree using the entire training dataset (Tripathi and Tiwari, 2022). Bootstrap sampling generally reduces the variability and systematic error of the dataset. The RF algorithm has been extensively studied in the remote sensing literature over the past few decades due to its reputation as one of the most efficient classifiers (Bousbih et al., 2019). This algorithm has various applications in agriculture, such as soil texture classification and analysis. Creating an RF classifier involves constructing classification and regression trees (CARTs) using the provided samples (Bousbih et al., 2019). Three critical parameters influence the effectiveness of the RF classifier: the number of trees (K), which typically leads to more accurate results; the maximum depth of each tree, which is limited to 25, and the minimum number of samples in each node (Bousbih et al., 2019).

Maximum likelihood classifier. The maximum likelihood classifier (ML) is a prominent parametric statistical technique in remote sensing applications. In this method, analysts define training zones, which are representative regions, to facilitate the categorization process (Mustapha et al.,2010). Modern maximum likelihood classifiers assess the "likelihoods" of relative class membership for individual pixels within an image by incorporating information from all training sets. The probability density function of each class, considering the likelihood of a pixel belonging to that specific class, is utilized to assign pixels to their respective classes during classification (Lillesand et al., 2015).

RESULTS AND DISCUSSION

Particle size analysis

The particle size analysis is applied of the thirteen soil samples, it was observed that the percentage of gravel was generally low in the majority of samples, ranging from 0% to 8%, except for three sites where the percentage of gravel was notably higher at 21.3%, 34.7%, and 38.1%.The results for the sand content varied from 2.32% to 25.86%, with only two locations showing significantly higher sand percentages of 55.24% and 50.02%, respectively. Silt emerged as the dominant component in most cases.

Atterberg limits

The boundary defining the various physical states of sediments was established using the Atterberg limits. The findings from the Atterberg limits revealed that the liquid limit (LL) ranged from 19.8% to 31.2%, with an average of 25.95%. The plastic limit (PL) varied from 0% to 17.5%, with an average of 8.66%. The plasticity index (PI), which is the difference between the liquid limit and the plastic limit, ranged from 5.4% to 29.5%. Most of the soil samples exhibited a significant presence of silt, leading to plasticity index values falling within the low to moderate levels.

Statistical analysis

Figures 4 illustrate and explains the backscattering characteristics of C-band SAR in different polarizations, showing the representation of soil roughness bands with various surface features.

In Figure 4, the density value exhibits a relatively high consistency with the backscatter coefficient in dual polarization data used VH and VV, whereas in the moisture value does not demonstrate the same level of consistency as seen in the density case.

Classification of soil using texture triangles

Soil texture refers to the arrangement of mineral particles within the soil based on their size. According to the USDA (United States Department of Agriculture) classification, clay refers to particles with a diameter less than 2 µm, silt refers to particles with a diameter between 2 and 50 µm, and sand refers to particles with a diameter of 0.05 to 2 mm. The measured clay content ranged from 0% to 14%, while the sand content ranged from 2.32% to 55.24% based on ground measurements of the soil samples. In Figure 5, we can see

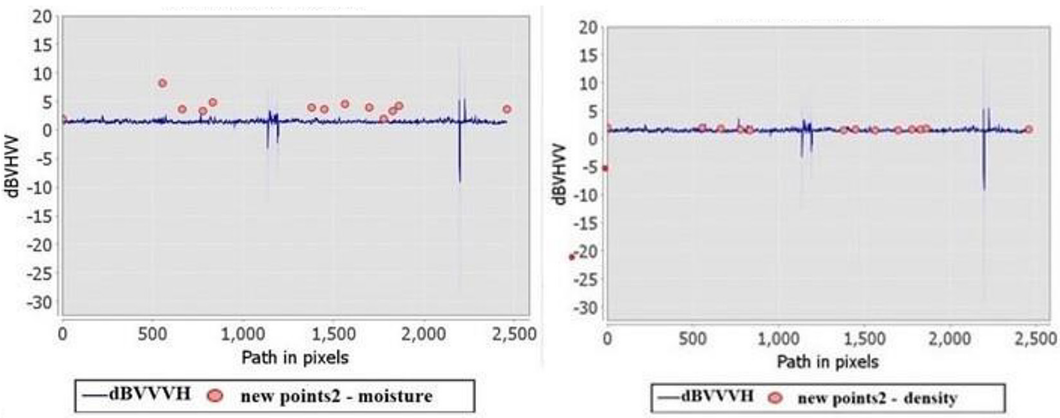

Figure 4. Profile plot for density and moisture

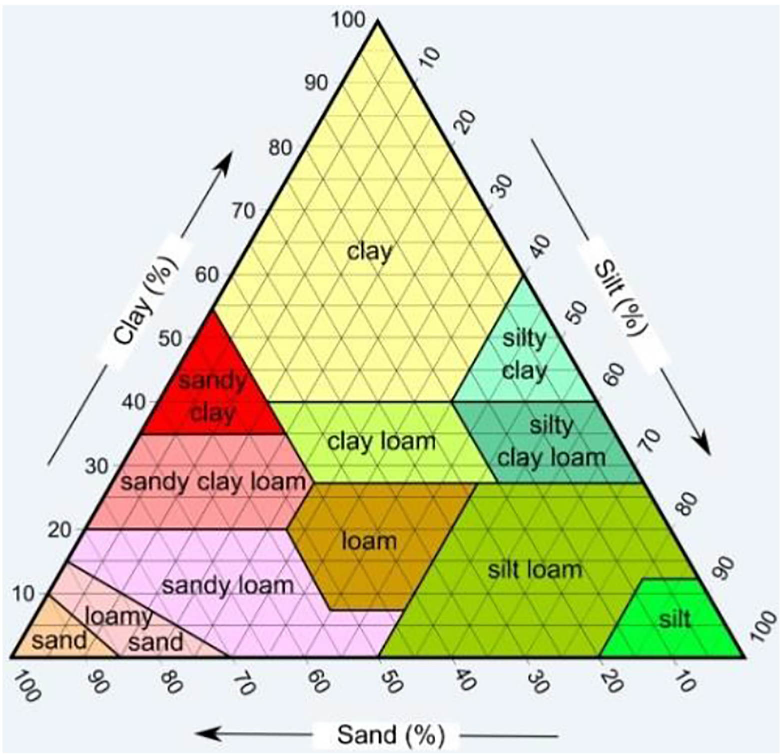

Figure 5. Soil texture triangle classification

the assessed and classified field findings according to the soil texture triangle categorization. The classification includes five main soil types: sandy clay with gravel, silt, silt loam, silt clay loam, and silt loam with gravel.

Validation and model generation

A linear regression model was utilized to establish relationships and characterize the physical Attributes of the soil parameters. Table 1 presents the associations between various soil properties, including soil texture (gravel, sand, silt, and clay), Atterberg limits (liquid limit, plastic limit, and plasticity index), water content, and dry density. The correlation analysis indicated that dry density was not significantly correlated with the other parameters. However, weak positive correlations were observed between the water content and the liquid limit (0.111), plastic limit (0.041), and plasticity index (0.152). Additionally, a weakly positive association was found between the liquid limit and plastic limit (0.222), and a very weak link was observed between the liquid limit and plasticity index (0.002).Significant positive correlations were identified between the plasticity index and the silt content (0.817) and clay content (0.952).

Figures 6 to 8 present examples showing the correlation coefficients between the examined soil parameters calculated through SPSS software

Table 1. Relationships between the physical properties of the soil parameters

Parameter	Water content	Dry density	L.L	P.L	P.I	Gravel%	Sand%	Silt%	Clay%
Water content	1								
Dry density	0.035	1							
L.L	0.111	0.143	1						
P.L	0.041	0.006	0.222	1					
P.I	0.152	0.009	0.002	0.817	1				
Gravel%	0.001	0.352	0.018	0.032	0.019	1			
Sand%	0.045	0.212	0.001	0.029	0.031	0.736	1		
Silt%	0.166	0.122	0.079	0.004	0.004	0.859	0.952	1	
Clay%	0.002	0.058	0.012	0.005	0.001	0.121	0.012	0.007	1

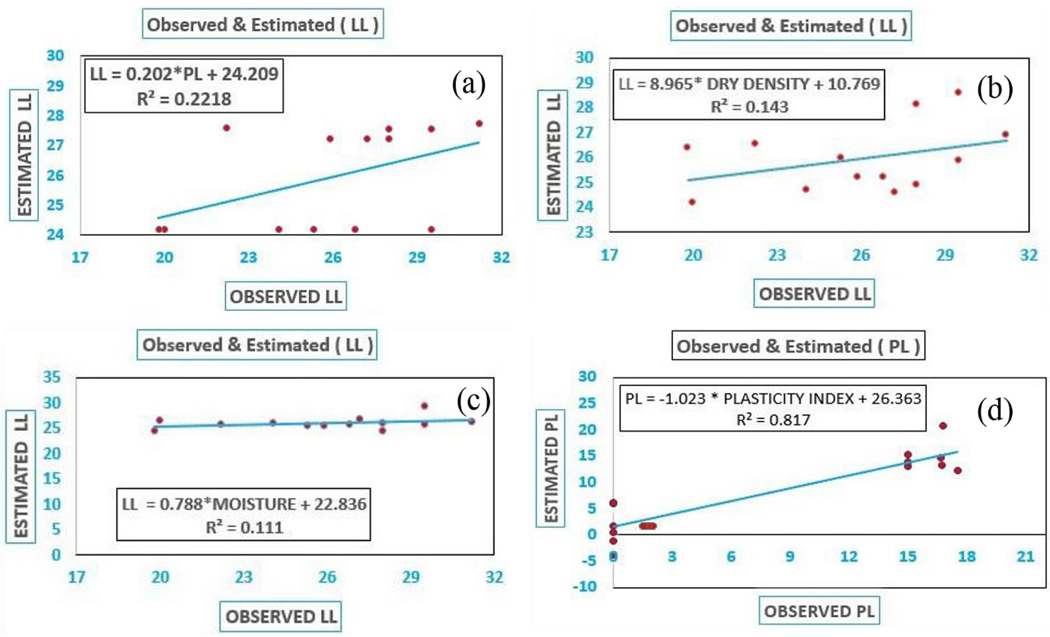

Figure 6. Correlation liquid limit wiht (a) plastic limit (b) dry density (c) moisture, (d) correlation PL & PI

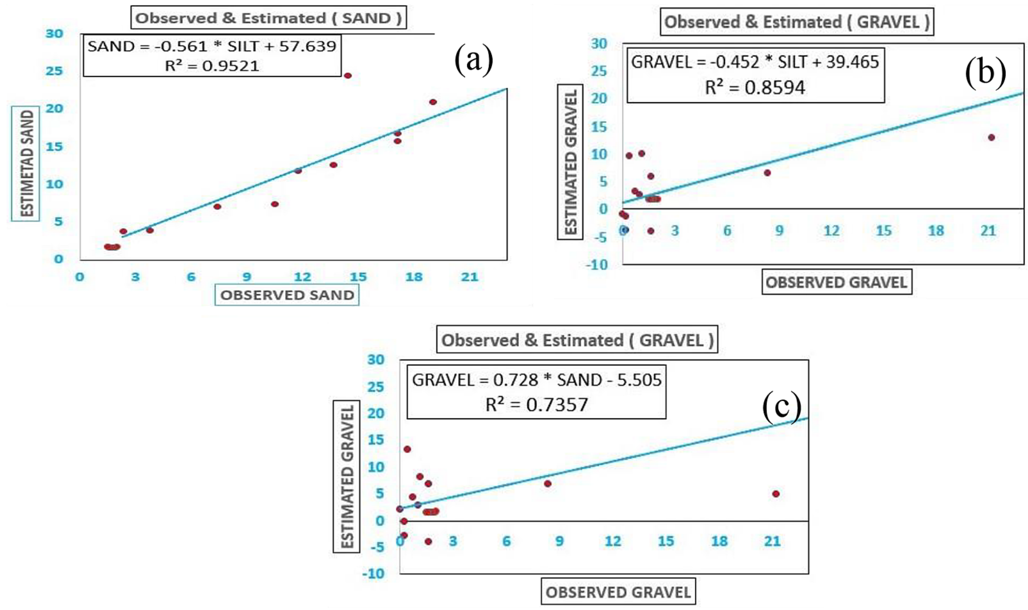

Figure 7. (a) Correlation sand & silt, correlation gravel with (b) silt (c) sand

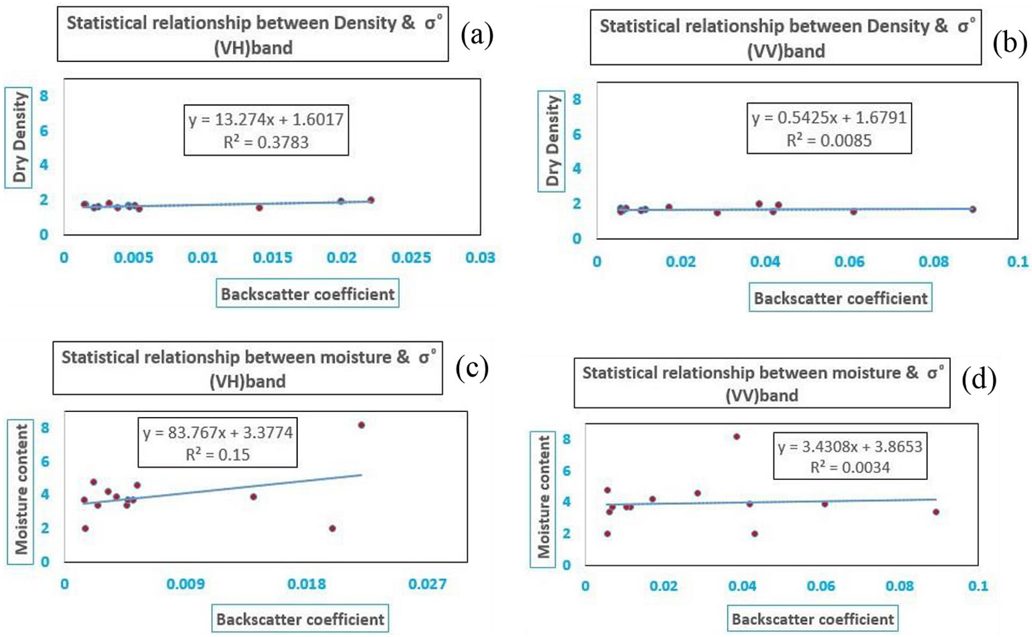

Figure 8. Relationship between σ° and density: (a) in (VH) and (b) in (VV), Relationship between σ ° and moisture: (c) in (VH) and (b) in (VV)

using the linear regression model. These figures include the dependent and independent equations, as well as the R-value, which represents the strength of the correlation. The empirical regression equations derived from these correlations can offer initial insights into certain characteristics of the soil parameters under investigation.

The analysis of density shows that the VH band is better for calculating its backscatter coefficients while, the moisture analysis show the (VH) band is better. As a result, the (VH) band is better for both cases to calculate their backscatter. The soil triangle as shown in (Figure 5) featuring the axes of sand, silt, and clay percentages led to the identification of various soil subcategories. These subcategories include silt (47.49%), silt loam with gravel (32.97%), sandy clay with gravel (5.51%), silt loam (11.604%), and silt clay loam (2.41%). These percentages were obtained through the random forest method. Approximately 13 soil samples were superimposed on the

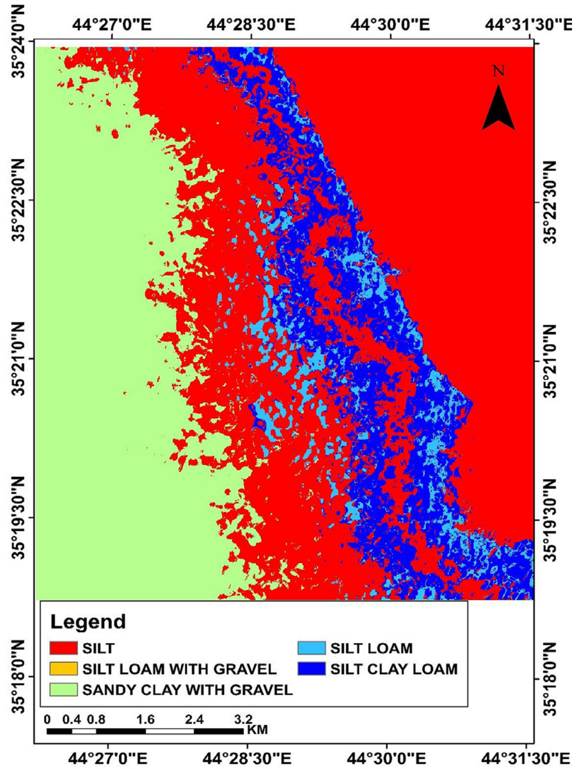

Figure 9. The soil category map of the study region derived from the modified soil textural triangle of the SAR parameters using RF

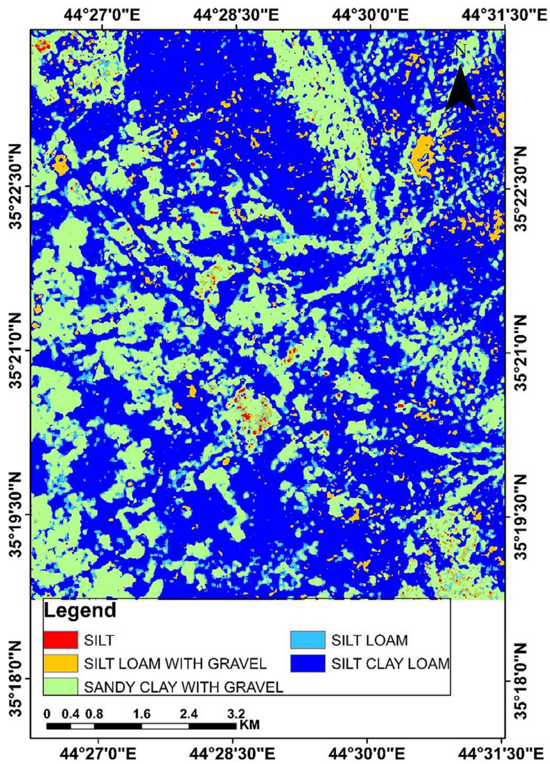

Figure 10. The soil category map of the study region derived from the modified soil textural triangle of SAR parameters using ML

Table 2. Confusion matrix for the classifications

Reference label percentage	Random forest method	Maximum likelihood	Overall accuracy and kappa coefficient
Silt	47.49%	5.911	Random forest method OA=0.801886792 Kappa=0.750588235 Maximum likelihood OA = 0.9625 Kappa= 0.95
Silt loam with gravel	32.97%	80.596	
Sandy clay with gravel	5.51%	0.982	
Silt loam	11.604%	12.512	
Silt clay loam	2.41%	0	

map, indicating the percentages of each class. The maximum likelihood method exhibits superior accuracy across different metrics. Nonetheless, comparable results are observed between the RF and ML methods. This research utilizes a restricted feature set for classification inputs, highlighting the need to expand sample sizes for validation. Moreover, the computation time during the learning process serves as a significant factor in comparing algorithms.

CONCLUSION

The study effectively developed models for estimating topsoil properties by analyzing parametric and textural features extracted from Sentinel-1 C-SAR (VV, VH) images. Field measurements collected from 13 soil samples in the Laylan region of Kirkuk City, Iraq, were utilized to develop and validate these models. The classification algorithms, including RF and ML classifiers, employed specific indicators derived from Sentinel-1 data. Additionally, a soil triangle, constructed using three axes to represent the predicted target parameters, facilitated the identification of five distinct soil groups in the study area.

The results revealed that the soil triangle adeptly delineated five distinct subcategories of soil, each characterized by unique proportions of sand and silt. Soil samples were meticulously categorized into one of five predefined classes based on their clay content, which ranged from 0% to

14.48%. The performance assessment of the ML and RF algorithms showcased their prowess in estimating percentage labels, even with limited training data. Notably, the ML algorithm outperformed the RF, exhibiting higher accuracy in the classification task.

These models and methodologies exhibit significant promise for soil texture classification using SAR imaging. However, their true potential can only be realized through testing across diverse geographic regions with varying climatic conditions. Future research could expand on these findings by using these models to generate comprehensive soil texture maps, thereby enhancing soil parameter estimation in a variety of environments.

REFERENCES

1. Alexandridis, T.K., Cherif, I., Bilas, G., Almeida, W.G., Hartanto, I.M., Andel, S.J.V., Araujo, A. 2016. Spatial and temporal distribution of soil moisture at the catchment scale using remotely-sensed energy fluxes. Water 8(1), 32.
2. Amin B.P. 2022. Delineate the hydrological boundaries situation using the morphometric analysis and geological features: A case study of laylan sub-basin, Kirkuk / NE Iraq. IOP Conference Series: Earth and Environmental Science 1120(1).
3. Bousbih, Sribi, M., Pelletier, C., Gorrab, A., Lili--Chabaane, Z., Baghdadi, N., Aissa, N.B., Mougenot, B. 2019. Soil texture estimation using radar and optical data from Sentinel-1 and Sentinel-2. Remote Sensing 11(13).
4. Breiman, L. 2001. Random Forests. Machine learning 45, 5–32.
5. Chang, D.-H., Kothari, R. and Islam S. 2003. Classification of soil texture using remotely sensed brightness temperature over the southern great plains. IEEE transactions on Geoscience and Remote Sensing 41(3), 664–74.
6. Robertson, L.D., Davidson, A.M., McNairn, H., Hosseini, M., Mitchell, S., de Abelleyra, D., Verón, S., le Maire, G., Plannells, M., Valero, S., Ahmadian, N., Coffin, A., Bosch, D., Cosh, M.H., Basso, B., Saliendra, N. 2020. C-Band synthetic aperture radar (SAR) imagery for the classification of diverse cropping systems. International Journal of Remote Sensing 41(24), 9628–49. https://doi.org/10.1080/01431161.2020.1805136
7. Robertson, L.D., Davidson, A., McNairn, H., Hosseini, M., Mitchell, S.W., de Abelleyra, D. Veron, S., Cosh, M.H. 2020. Synthetic aperture radar (SAR) image processing for operational space-based agriculture mapping. International Journal of Remote Sensing 41(18), 7112–44.
8. Ge, Y., Thomasson, J.A. and Sui, R. 2011. Remote sensing of soil properties in precision agriculture: A review. Frontiers of Earth Science 5, 229–38.
9. Grimm, R., Behrens, T., Märker, M., and Elsenbeer H. 2008. Soil organic carbon concentrations and stocks on barro Colorado Island—Digital soil mapping using random forests analysis. Geoderma 146(1–2), 102–13.
10. Holah, N., Baghdadi, N., Zribi, M., Bruand, A., King, C. 2005. Potential of ASAR/ENVISAT for the characterization of soil surface parameters over bare agricultural fields. Remote sensing of environment 96(1), 78–86.
11. Huang, H.H. and He Q. 2022. Nonlinear regression analysis. International Encyclopedia of Education: Fourth Edition 3, 558–67.
12. Kornelsen, K.C, and Coulibaly, P. 2013. Advances in soil moisture retrieval from synthetic aperture radar and hydrological applications. Journal of Hydrology 476, 460–89.
13. Korres, W., Reichenau, T.G., Fiener, P., Koyama, C.N., Bogena, H.R., Cornelissen, T., Baatz, R., Herbst, M., Diekkrüger, B., Vereecken, H. Schneider, K. 2015. Spatio-temporal soil moisture patterns–A meta-analysis using plot to catchment scale data. Journal of hydrology 520, 326–41.
14. Liao, K., Xu, S., Wu, J., and Zhu, Q. 2013. Spatial estimation of surface soil texture using remote sensing data. Soil science and plant nutrition 59(4), 488–500.
15. Lillesand, T., Kiefer, R.W. and Chipman, J. 2015. Remote Sensing and Image Interpretation. John Wiley & Sons.
16. Loew, A., and Mauser, W. 2007. Generation of geometrically and radiometrically terrain corrected SAR image products. Remote Sensing of Environment 106(3), 337–49.
17. Mustapha, M., Lim, H.S., Jafri, M.Z.M. 2010. Comparison of neural network and maximum likelihood approaches in image classification.
18. Mahmoud, A.S., Mezaal, M.R., Hameed, M.R., and Naje A.S. 2022. A Framework for improving urban land cover using object and pixel-based techniques via remotely sensed data. Nature Environment & Pollution Technology 21.
19. Ridha, M.M., Mahmoud, A.S., Jasim, M.A., and Naje, A.S. 2022. Dynamics of land use and land cover change using geospatial techniques–A case study of Baghdad, Iraq. Ecological Engineering & Environmental Technology 23.
20. Periasamy, S. 2018. Significance of dual polarimetric synthetic aperture radar in biomass retrieval: An attempt on Sentinel-1. Remote Sensing of Environment 217, 537–49.
21. Periasamy, S., Senthil, D. and Shanmugam, R.S. 2021. A soil texture categorization mapping from

empirical and semi-empirical modelling of target parameters of synthetic aperture radar. Geocarto International 36(5), 581–98. https://doi.org/10.1080/10106049.2019.1618924.

22. Salahalden, V.F., Shareef, M.A. and Al Nuaimy, Q.A. 2024. Red clay soil physical and chemical properties distribution using remote sensing and GIS techniques in Kirkuk City, Iraq. Iraqi Geological Journal 57(1), 194–220.
23. Shareef, M.A., Toumi, A. and Khenchaf, A. 2014. Prediction of water quality parameters from SAR images by using multivariate and texture analysis models. SAR Image Analysis, Modeling, and Techniques XIV 9243(October 2014), 924319.
24. Souissi, B., and Ouarzeddine, M. 2016. Polarimetric SAR data correction and terrain topography measurement based on the radar target orientation angle. Journal of the Indian Society of Remote Sensing 44, 335–49.
25. Srivastava, H.S., Patel, P., Sharma, Y., and Navalgund, R.R. 2009. Large-area soil moisture estimation using multi-incidence-angle RADARSAT-1 SAR data. IEEE Transactions on Geoscience and Remote Sensing 47(8), 2528–35.
26. Tripathi, A., and Tiwari, R.K. 2022. Utilisation of spaceborne c-band dual pol Sentinel-1 SAR data for simplified regression-based soil organic carbon estimation in Rupnagar, Punjab, India. Advances in Space Research 69(4), 1786–98. https://doi.org/10.1016/j.asr.2021.08.007
27. Yu, H., Kong, B., Wang, G., Du, R., Qie, G. 2018. Prediction of soil properties using a hyperspectral remote sensing method. Archives of Agronomy and Soil Science 64(4), 546–59.
28. Zou, K.H., Tuncali, K., and Silverman, S.G. 2003. Correlation and simple linear regression. Radiology 227(3), 617–28.
29. van Zyl, J.J, Chapman, B.D., Dubois, P., and Shi, J. 1993. The effect of topography on SAR calibration. IEEE Transactions on Geoscience and Remote Sensing 31(5), 1036–43.